2020

Dropsonde Observations of the Ageostrophy within the Pre-Cold-Frontal Low-Level Jet Associated with Atmospheric Rivers

Rueben Demirdgian
Scripps Institution of Oceanography

Joel R. Norris
Scripps Institution of Oceanography

Andrew Martin
Portland State University

F. Martin Ralph
Scripps Institution of Oceanography

Citation Details

Demirdgian, Rueben; Norris, Joel R.; Martin, Andrew; and Ralph, F. Martin, "Dropsonde Observations of the Ageostrophy within the Pre-Cold-Frontal Low-Level Jet Associated with Atmospheric Rivers" (2020). Monthly Weather Review, 148, 1389-1406.

Dropsonde Observations of the Ageostrophy within the Pre-Cold-Frontal Low-Level Jet Associated with Atmospheric Rivers

REUBEN DEMIRDJIAN AND JOEL R. NORRIS

Center for Western Weather and Water Extremes, and Climate, Atmospheric Science and Physical Oceanography Division, Scripps Institution of Oceanography, La Jolla, California

ANDREW MARTIN

Department of Geography, Portland State University, Portland, Oregon

F. MARTIN RALPH

Center for Western Weather and Water Extremes, and Climate, Atmospheric Science and Physical Oceanography Division, Scripps Institution of Oceanography, La Jolla, California

(Manuscript received 26 July 2019, in final form 17 January 2020)

ABSTRACT

The pre-cold-frontal low-level jet (LLJ) is an important contributor for water vapor transport within atmospheric rivers, though its dynamics are not completely understood. The present study investigates the LLJ using dropsonde observations from 24 cross-atmospheric river transects taken during the CalWater-2014, 2015 and the AR-Recon 2016, 2018 field campaigns. It is found that the LLJ, located at ~1-km elevation ahead of the cold front, has an average maximum wind speed of 30 m s^{-1} and is strongly supergeostrophic with an average ageostrophic component of 6 m s^{-1}. The alongfront ageostrophy occurs within the atmospheric layer (750–1250 m) known to strongly control orographic precipitation associated with atmospheric rivers. The ERA5 reanalysis product is used to both validate the observed *geostrophic* winds and investigate the supergeostrophic jet dynamics. The comparison demonstrates that there is no systematic bias in the observed geostrophic wind but that the ERA5 LLJ total wind field is generally biased low by an amount consistent with the observed ageostrophy. One of the few cases in which the ERA5 produces an ageostrophic LLJ occurs on 13 February 2016, which is used to investigate the dynamical processes responsible for the ageostrophy. This analysis demonstrates that the isallobaric (pressure tendency) term serves to accelerate the ageostrophic jet, and the Coriolis torque and advective tendency terms serve to propagate the jet normal to the LLJ. Therefore, if a model is to accurately represent the LLJ, it must adequately resolve processes contributing toward the pressure tendencies along the cold front.

1. Introduction

The pre-cold-frontal low-level jet (LLJ) is a key feature associated with atmospheric rivers (ARs) that accompany extratropical cyclones (Ralph et al. 2005, 2017; Neiman et al. 2008; Guan and Waliser 2015; Dettinger et al. 2011; Dettinger 2013; Lavers et al. 2011; Moore et al. 2012; Rutz et al. 2014; American Meteorological Society 2017). The LLJ typically exhibits a moist neutral stratification, modest vertical wind shear, and a mean wind speed maximum of approximately 30 m s^{-1} at 1-km elevation (Browning and Pardoe 1973; Ralph et al. 2005; Kingsmill et al. 2013). A landfalling AR with an embedded LLJ can produce copious precipitation from even modest orographic lift (~250 m), as often seen in the winter season for the West Coast of the United States, because they are regions of large water vapor content with very little vertical displacement required for saturation (Ralph et al. 2005, 2006; Dettinger et al. 2011; Kingsmill et al. 2013; Valenzuela and

Denotes content that is immediately available upon publication as open access.

Supplemental information related to this paper is available at the Journals Online website: https://doi.org/10.1175/MWR-D-19-0248.s1.

Corresponding author: Reuben Demirdjian, rdemirdjian@ucsd.edu

DOI: 10.1175/MWR-D-19-0248.1

Kingsmill 2015). The LLJ substantially contributes to the total moisture transport at an elevation of 750–1250 m, dubbed the controlling layer (Neiman et al. 2002, 2009), which is found to be highly correlated with U.S. West Coast orographic precipitation. Despite its clear relevance, Martin et al. (2018) found a low bias in the LLJs water vapor transport for both the WRF and GEFS reforecasts models compared with flight dropsondes.

The earliest investigations that recognized the ageostrophy associated with the LLJ came from analyses of the thermal wind imbalance, the difference between the thermal wind shear and the actual wind shear, across cold fronts. Orlanski and Ross (1977) performed a two-dimensional dry idealized numerical study to investigate the degree of geostrophic balance in the cold frontal region and found an imbalance within a narrow region ahead of the cold front. They attributed the thermal wind imbalance to the circulation arising from the symmetric instability that ''advects [along front] momentum and potential temperature at different rates, thereby producing a geostrophic imbalance.'' Thorpe and Clough (1991) verified this in observations by performing the same calculation on dropsonde transects across several LLJs. Moreover, they found that a strong mesoscale thermal wind imbalance occurred ahead of the cold front while outside of that region conditions were largely in a state of thermal wind balance. The dynamical interpretations were limited in these two studies, however, because the former was a dry idealized 2D simulation and the latter was based on observations that are instantaneous snapshots of the circulations.

Diagnostic studies of the evolving transverse circulation associated with the upper-level jet streak were later performed by Uccellini and Johnson (1979) and Brill et al. (1985). Both performed case study simulations to diagnose the low-level wind field resulting from the propagating upper-level jet streak using a framework based on mass and momentum adjustment. They each found linkages between the upper-level and lower-level flow with the isallobaric wind driving the ageostrophy within the LLJ. Winters and Martin (2014) performed a similar but more quantitative analysis by calculating the ageostrophic transverse circulation using the Sawyer–Eliassen equation and found that the contribution of the LLJ to the moisture flux had a substantial impact on the 2010 Nashville, Tennessee, flooding event.

A similar but different framework to determine the contributing mechanisms driving the ageostrophic LLJ can be made by rearranging the expression for horizontal momentum and then solving for the ageostrophic wind tendency. The resulting three forcing terms are associated with momentum advection, Coriolis torque of the ageostrophic wind, and isallobaric component. Dudhia (1993) simulated a real event that resolved the ageostrophy of the LLJ and speculated that it resulted from the Coriolis torque on the thermally direct cross frontal flow. Chen et al. (1994) performed a diagnostic case study analysis of a LLJ using a combination of soundings and analysis data. They found that the isallobaric term dominated the momentum advection term, though their formulation of the momentum equations did not include the Coriolis torque of the ageostrophic winds. Notably, however, they ruled out the vertical mixing of momentum as a mechanism within their LLJ. Wakimoto and Murphey (2008) utilized flight dropsonde transect observations across a LLJ combined with a scaling argument to assert that the along-frontal ageostrophy is a result of the isallobaric wind component associated with the propagation of a cyclone. The differing dynamical mechanisms accounted for in these studies indicate that there are either several different processes leading to the production of the ageostrophy in a LLJ or that some of the analyses are insufficient in some regard.

While the studies mentioned above discuss the ageostrophy of the LLJ, they all do so only for a small number of very intense cases. Consequently, the general characteristics of this feature are not well documented in the literature, such as its average contribution to the total wind strength. Moreover, it is not known whether ageostrophy is present among a variety of LLJs or only in the most intense ones. From a predictability perspective, it is important to understand the dynamical origins of the ageostrophy because it contributes a substantial fraction of the water vapor transport that can lead to orographic precipitation. Therefore, the accuracy of a precipitation forecast depends at least partially upon the model resolving the ageostrophic component of the transport. Furthermore, none of the existing studies evaluate a model representation of the LLJ ageostrophy against direct observations.

To address these issues, this study (i) introduces a comprehensive observational approach to many more cases than have been examined in previous studies, (ii) includes cases of varying LLJ intensity, (iii) compares the observations to the new ERA5 reanalysis to check for systematic biases, and (iv) investigates the ageostrophic dynamics in a case study. The model validation of the ageostrophy is an important step forward because it can identify any systematic biases in LLJ wind that may be present in the reanalysis. This study is partitioned in the following way. Section 2 describes the data and methods, section 3 discusses the observed ageostrophic component of the LLJ and its validation with the ERA5 reanalysis product, section 4 presents a

TABLE 1. The aircrafts used, dates, times, and locations of 24 dropsonde cases as well as some results unique to this study. The full names of the G-IV and C-130 aircrafts are the Gulfstream G-IV SP, N49RF, and the ARFC C-130 J.

Transect [yyyymmddT#]	Aircraft	First sonde [hh:mm]	Last sonde [hh:mm]	No. of sondes	Height of LLJ [m]	LLJ wind speed [m s^{-1}]	Max AgLLJ [m s^{-1}]	MAX IVT [kg m^{-1} s^{-1}]	Vag/wspd
20140208T1	G-IV	20:50	21:46	9	400	23	8	638	0.35
20140208T2	G-IV	22:43	23:38	9	800	27	5	946	0.19
20140211T1	G-IV	19:03	21:03	14	1200	44	9	1171	0.2
20140211T2	G-IV	20:33	21:24	12	1500	42	4	1041	0.1
20140213T1	G-IV	18:51	20:22	16	1500	30	2	733	0.07
20150115T1	G-IV	21:14	22:46	12	700	31	8	656	0.26
20150117T1	G-IV	22:45	0:30	10	500	32	12	749	0.38
20150206T3	G-IV	21:59	22:59	8	1000	31	9	886	0.29
20150208T2	G-IV	13:12	14:48	13	1000	27	−2	871	−0.07
20150214T1	G-IV	18:03	19:28	13	1000	30	1	1048	0.03
20160213T1	C-130	20:41	23:41	20	400	29	6	662	0.21
20160213T2	C-130	23:41	1:58	23	1500	37	4	848	0.11
20160213T3	C-130	20:33	23:21	25	500	33	9	655	0.27
20160215T1	C-130	20:47	23:01	16	900	29	5	516	0.17
20160215T2	C-130	23:01	2:02	20	1200	32	6	229	0.19
20160221T2	C-130	20:33	0:00	23	1500	41	−5	714	−0.12
20180126T2	C-130	0:15	1:46	8	700	27	2	580	0.07
20180126T3	C-130	20:44	22:22	10	400	24	12	439	0.5
20180128T1	C-130	20:31	21:34	6	600	33	6	870	0.18
20180128T2	C-130	21:34	23:04	7	1100	33	7	731	0.21
20180128T4	C-130	0:36	1:36	6	600	21	5	547	0.24
20180131T3	C-130	20:31	23:02	16	1400	33	−11	696	−0.33
20180202T3	C-130	20:34	23:57	17	400	28	7	675	0.25
20180202T5	G-IV	20:58	22:18	12	800	40	8	888	0.2

case study of the dynamics associated with the ageostrophic component of the LLJ, and section 5 contains the conclusions and discussion.

2. Data and methods

a. Dropsondes

The primary dataset used in this study is a collection of 1239 aircraft dropsonde profiles of which 325 met our criteria from 24 flight transects through 15 different ARs obtained during intensive observing periods (IOPs) conducted in the northeastern Pacific over a 5-yr period (Table 1). These IOPs and their aircraft include the NOAA G-IV for CalWater 2014–15 and two C-130s from the U.S. Air Force 53rd Weather Reconnaissance Squadron for AR-Recon 2016 (Ralph et al. 2016, 2017; Cordeira et al. 2017), and two Air Force C-130s and the NOAA G-IV for AR-Recon 2018. The dropsondes measured wind, relative humidity, temperature, and pressure with uncertainties of 1.5 m s^{-1}, 2%, 0.2 K, and 0.4 hPa, respectively (Vaisala RD94 data sheet; Vaisala engineer, Frank DeFina 2018, personal communication). The dropsondes were released from an elevation between 8 and 10 km and each transect took about 1 h, depending on the length of the transect, with an average of 7 min between dropsondes.

The case list of the LLJs was selected based on the following criteria: (i) a low-level wind speed maximum must be present at or below 1500 m, the maximum observed height of a LLJ, (ii) a cold front (identified through examination of the potential temperature transects) must be present in the transect to ensure a pre-cold-frontal-type LLJ, (iii) each transect must have at least two dropsondes on both sides of the LLJ center, defined by the maximum in wind speed, so that center finite differencing can be used, (iv) the latitude of LLJ must be greater than 20°N to exclude tropical events, and (v) transects occurring on the same flight day must meet a case independence criterion to prevent unequal weighting of similar transects. Criterion (v) was enforced by comparing the root-mean-square error (RMSE) of wind speed from the relevant transect with respect to all other transects that met criteria (i)–(iv), and transects from the same day were determined to be independent if the RMSE of same-day transects was greater than the minimum RMSE with respect to all other transects. Informally speaking, this means that two transects taken on the same day are objectively determined to have greater differences in comparison to transects taken across completely different ARs.

Once the case list was compiled, processing of the dropsondes was done in four stages. In the first stage,

NCAR's Atmospheric Sounding Processing Environment (ASPEN) software was used to quality control the data (https://www.eol.ucar.edu/content/aspen), which was done by the aircraft crew members prior to sending them out to be used by researchers. In the second stage, each dropsonde profile was regridded from its native vertical resolution (~20 m) to a fixed 100-m vertical grid between 0 and 8 km above mean sea level (approximately the lowest height of any of the aircraft) according to the arithmetic mean of all observations occurring within 50 m of each point in the grid. All state variables of every dropsonde profile were plotted (not shown) and visually inspected and compared to the original raw profiles to ensure that no relevant information was lost (i.e., temperature inversions, wind maxima etc.).

In the third stage, the profile within each transect containing the strongest LLJ assessed by maximum wind speed was identified and defined as the transect center, hereafter referred to as the LLJ profile. For any case with double LLJs, the stronger among the two was selected to be the LLJ profile. The remaining dropsondes of the transects were time-to-space (T-S) adjusted following Neiman et al. (2014) with the assumption of a steady translation velocity during the measurement period. This T-S adjustment shifted the dropsonde locations to their positions at the time of the LLJ profile and caused a slight rotation in the sonde transect depending on the direction of flight (clockwise for an equatorward flight and counterclockwise for a poleward flight track).

Finally, in the fourth stage, the transects were regridded using linear interpolation along an 800-km transect centered at the LLJ profile with a spacing of 60 km (the average spacing between the dropsondes). The coordinates were then rotated to the transect normal axis (y', approximately the along-jet axis, as discussed later) and the along transect axis (x', across-jet axis). Note that the transect normal axis is very nearly along the direction of water vapor transport (Ralph et al. 2005) and approximately parallel to the cold front, which is typically oriented from the southwest to the northeast. Similarly, the transect parallel direction is approximately perpendicular to the direction of water vapor transport and is usually oriented from the northwest to the southeast.

The transect-normal geostrophic wind (v_g') was calculated using centered finite differencing and is given by

$$v_g' = \frac{1}{f\rho}\frac{\Delta p}{\Delta x}, \tag{1}$$

where f is the Coriolis parameter at the dropsonde latitude, ρ is the density as a function of height, Δp is the along-transect difference in pressure, Δx is the dropsonde spacing, and the prime superscript indicates a coordinate rotation. The transect-normal ageostrophic win (v_{ag}') was calculated from the residual between the transect-normal total wind and the transect-normal geostrophic wind. The measurement error of the geostrophic and ageostrophic winds was calculated by using formal error propagation techniques according to the dropsonde measurement uncertainties given previously, and it was found to be $\pm 1.5\,\mathrm{m\,s^{-1}}$. The transect-parallel geostrophic wind cannot be calculated due to insufficient data in the transect-normal direction.

b. Reanalysis

The newest reanalysis product from the European Centre for Medium-Range Weather Forecasts, ERA5 (European Centre for Medium-Range Weather Forecasts 2017), provided four uses in the present study. These were (i) a synoptic-scale context for the 24 cases, (ii) a comparison with the observed total, geostrophic, and ageostrophic wind fields, (iii) an assessment of whether the pressure tendencies over the sampling period were small enough to make the stationarity assumption, and (iv) a diagnostic analysis of the ageostrophic component of the LLJ. The ERA5 product used in the present study is available at a 1-h intervals with a resolution of 0.25° × 0.25° globally and 37 levels irregularly spaced from 1000 to 1 hPa at 25-hPa spacing or finer.

c. Gradient wind

An estimate of the gradient wind was calculated from a combination of the observations and the ERA5 reanalysis. The gradient wind was found by first assuming no wind speed acceleration and then by solving the following equation (Brill 2014):

$$\frac{V_{\mathrm{grad}}^2}{R} + fV_{\mathrm{grad}} + \frac{1}{\rho}\frac{\partial p}{\partial n} = 0, \tag{2}$$

where V_{grad} is the gradient wind, R is the radius of curvature of a parcel trajectory, ρ is the air density, and $(\partial p/\partial n)$ is the pressure gradient normal to the trajectory. Since the observations are not exactly normal to the trajectory (see Fig. 1 transect compared with blue lines) we cannot calculate the total gradient wind; however, we can calculate the gradient wind in the transect normal direction by using $\partial p/\partial x = (\partial p/\partial n)\cos(\theta_{\mathrm{diff}})$ and $V_{\mathrm{grad}}^N = V_{\mathrm{grad}}\cos(\theta_{\mathrm{diff}})$ where $(\partial p/\partial x)$ is the along transect pressure gradient, V_{grad}^N is the transect normal (N) gradient wind, and θ_{diff} is the angle difference between the transect and the trajectory. Using

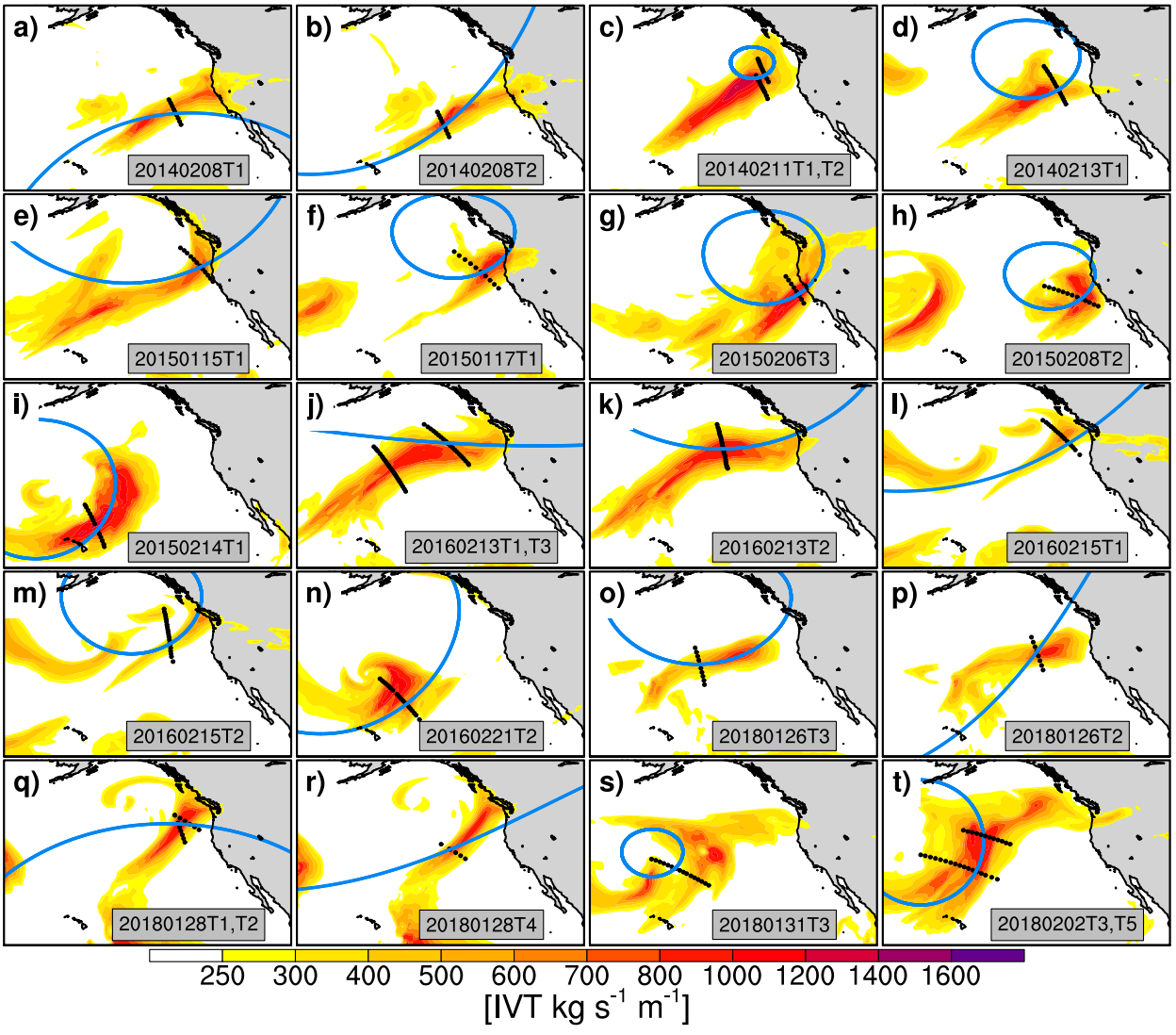

FIG. 1. Northeast Pacific plan view images of IVT (color fill; kg s^{-1} m^{-1}) from the ERA5 reanalysis product for each of the individual LLJ/AR cases. Black dots represent dropsonde locations and the blue curves show the radii of curvature for each LLJ trajectory. The flight transects are matched to the ERA5 plan view at the nearest 3 h interval. The bottom right text is the case identifier in the form yyyymmddT# where T# represents the transect number; cases with multiple transects on the same day have "T#" separated by commas.

these relationships, the gradient wind normal to the transect is given by the following equation:

$$\frac{(V^N_{\text{grad}})^2}{R\cos(\theta_{\text{diff}})} + fV^N_{\text{grad}} + \frac{1}{\rho}\frac{\partial p}{\partial x} = 0. \tag{3}$$

Following Brill (2014), the radius of curvature for parcel trajectories may be calculated using

$$R = -\frac{\Delta s}{\Delta\Theta}, \tag{4}$$

where Δs is the parcel displacement (straight-line distance between start and end points) and $\Delta\Theta$ is the change in wind direction from initial to final time. Using ERA5, a 15 min forward and backward trajectory centered at the LLJ dropsonde time was used to calculate R. The other quantities ($\partial p/\partial x$, f, and ρ) were all calculated from the dropsonde observations, and (3) was solved for the transect-normal gradient wind speed.

d. Stationarity

The stationarity assumption requires that the change in relevant quantities be sufficiently small during the sampling period such that the observations can be assumed to be taken at a single time. Since the focus of the paper is on the ageostrophic wind component, which was calculated by subtracting the geostrophic wind

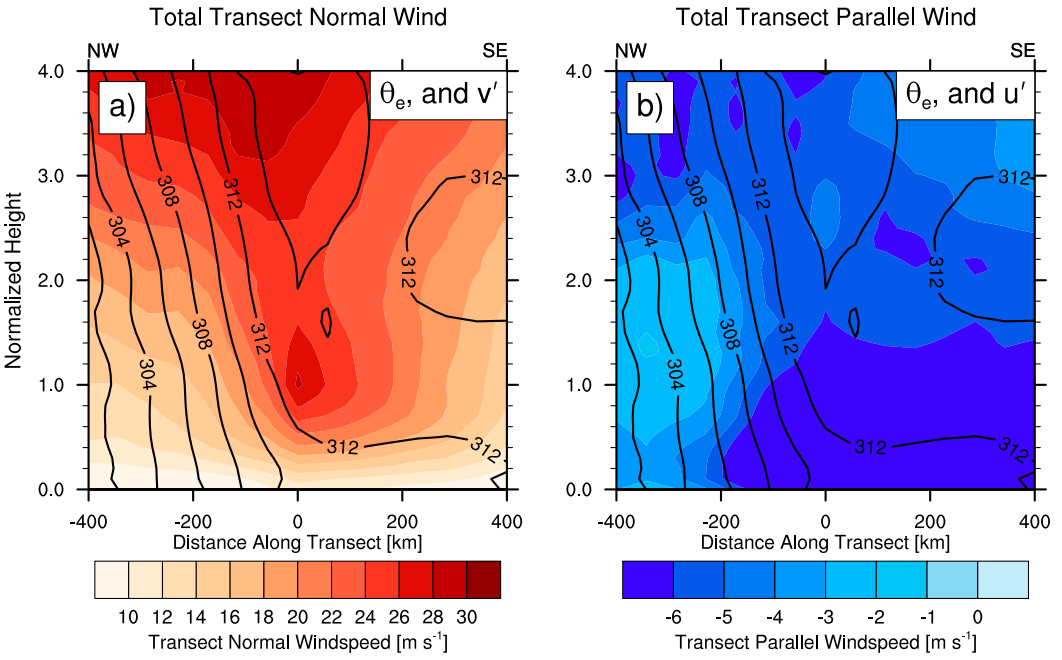

FIG. 2. Transect composites, normalized vertically by LLJ height, for (a) transect-normal (into the page) wind speed (color fill; m s^{-1}) and (b) transect-parallel (across the page) wind speed (color fill; m s^{-1}), with both plots having equivalent potential temperature (solid black; K).

component, it is imperative that the pressure tendencies be sufficiently small such that the geostrophic wind calculations were nearly unchanged during the observing period. The geostrophic wind centered finite difference method required three dropsonde profiles to be used, which took a total of 14 min on average for collection. The change in geostrophic wind was calculated at the LLJ profile by first calculating the pressure tendency in ERA5, then dividing by the model grid spacing to obtain the geostrophic wind tendency, and finally by multiplying it by the particular time it takes to release 3 dropsondes in each of the 24 transects. The result was an average change in the geostrophic wind of $\Delta v_g = 0.4\,\mathrm{m\,s^{-1}}$. Note that this is equivalent to taking the time tendency of (1) and multiplying by Δt. Since the result is much smaller than the observed ageostrophic winds (as will be shown), it follows that pressure-tendency corrections are not required since potential nonstationarity will not substantially bias the results presented here.

3. Observations of the ageostrophic component of the LLJ

a. Characterization

The 24 flight transects studied are overlaid onto their associated ARs in the thumbnail images in Fig. 1. Clearly, the set has substantial variety in terms of the AR strength, curvature, size, and latitude. The cases also have substantial variability in the strength of the LLJ (ranging from 21 to 44 m s^{-1}) as well as the height (ranging from 400 to 1500 m, Table 1). Despite this variety, the cases all feature transects across regions of strong water vapor transport.

The composite of the 24 transect-normal (v') and transect-parallel (u') wind fields, shown in Fig. 2, illustrates the characteristic environment within the AR. The vertical coordinate was normalized, prior to compositing, by dividing the true height by the LLJ height in each transect, thus creating unitless y axes in both Figs. 2 and 3. This procedure preserves the LLJ maximum, which would otherwise be smoothed out when LLJs of different heights were averaged together. However, the vertical coordinate can be approximately returned to dimensional units by multiplying the y axes by the average LLJ height (about 1000 m). A comparison of figures with normalized height (Figs. 2 and 3) and those without (not shown) indicates that important features such as the sharpness of the cold front are not drastically altered by the normalization process. For the purpose of display, a five-point local smoother was applied after all calculations were performed; comparison of smoothed and unsmoothed composites indicates that smoothing does not substantially alter the composites.

There are five apparent features worth noting in Fig. 2: (i) the intense LLJ of about 30 m s^{-1} centered at distance = 0 km and height = 1 and located on the warm

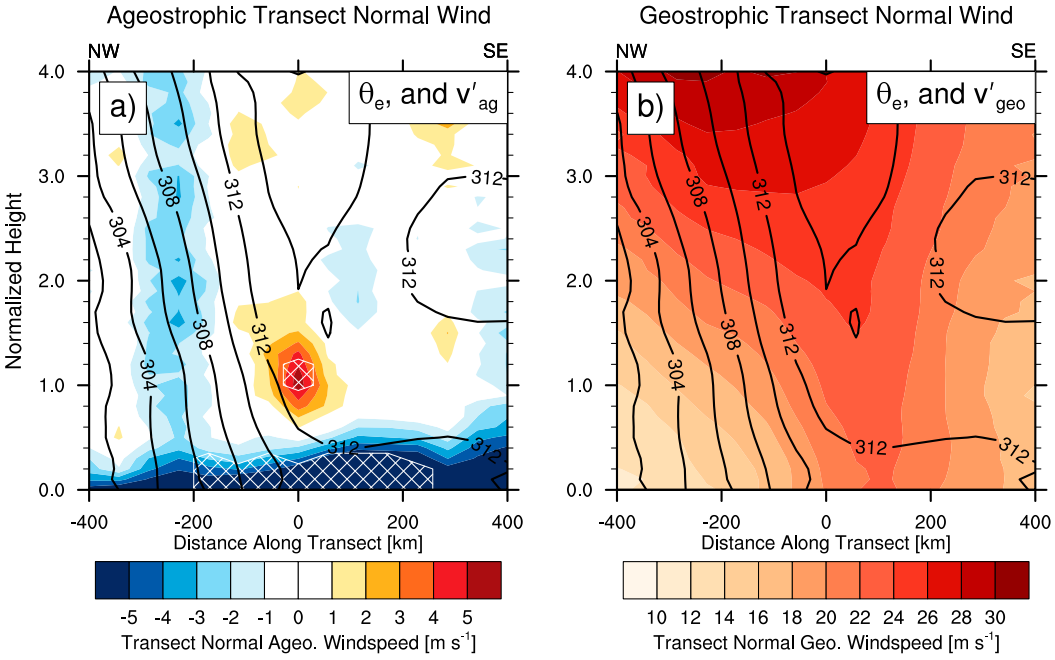

FIG. 3. Transect composites, normalized vertically by LLJ height, for the transect-normal (a) ageostrophic wind (color fill; m s^{-1}) and (b) geostrophic wind (color fill; m s^{-1}), with both plots having equivalent potential temperature (solid black; K). Hatching in (a) represents the 99.5th percentile of significance according to a binomial test (see text for details).

side of the cold front, (ii) a sharp equivalent potential temperature gradient seen on the cyclonic or northwest side of the LLJ marking both the cold front and moisture gradient, (iii) the region of low-level cross-frontal wind convergence on the cyclonic side of the LLJ at the cold frontal boundary (Fig. 2b), (iv) the much stronger horizontal wind shear on the cyclonic side of the LLJ relative to that on the anticyclonic side, and (v) the bottom of the upper-level jet streak above the cold front. It is important to note that features become smoothed in the composite such that they may become broader in scale and smaller in magnitude. However, the relative position of these features remains intact and the LLJ is observed immediately ahead of the cold front (Fig. 2a), as expected.

The composite ageostrophic wind shown in Fig. 3a was calculated by subtracting the transect normal wind (Fig. 2a) from the transect normal geostrophic wind (Fig. 3b) for each of the 24 transects individually, normalizing by height, and compositing using the same procedures described previously. One can readily draw four conclusions from Fig. 3: (i) the LLJ is supergeostrophic immediately ahead of the cold front; (ii) both the frontal zone and upper-level jet (not shown) are subgeostrophic, the latter being expected from gradient wind balance for flow around a trough; (iii) the near-surface wind is subgeostrophic, likely a result of frictional drag, though this is not substantiated in the present work; and (iv) the transect-normal flow is nearly in geostrophic balance outside of the regions mentioned in (i), (ii), and (iii). The composite transect indicates that the ageostrophic component of the LLJ (termed the AgLLJ) has a smaller transect-parallel width scale (≈100 km) than that of the AR (≈500 km). It is likely that the transect-normal length scale of the AgLLJ is similar to the length scale of the AR (on order of 1000 km) since, when combined, the transects collectively sample all areas along the AR (see Fig. 1). However, it cannot be ruled out that the ageostrophy occurs in most of the cases merely because each flight strategically targeted meteorologically similar regions of strong water vapor transport.

Two different statistical significance tests are applied to the AgLLJ feature. The first is a two tailed binomial distribution test using a 50% probability of success (either positive or negative ageostrophy) to determine the likelihood that the 21 of 24 cases of positive ageostrophy could have occurred by chance. The hatching in Fig. 3 shows the regions of statistical significance to the 99.5th percentile for this test, highlighting the extreme degree of confidence that the AgLLJ does not merely result from sampling variability (more information is provided in Fig. S1 in the online supplemental material). The second test is a two-tail standard Student's *t* test at the

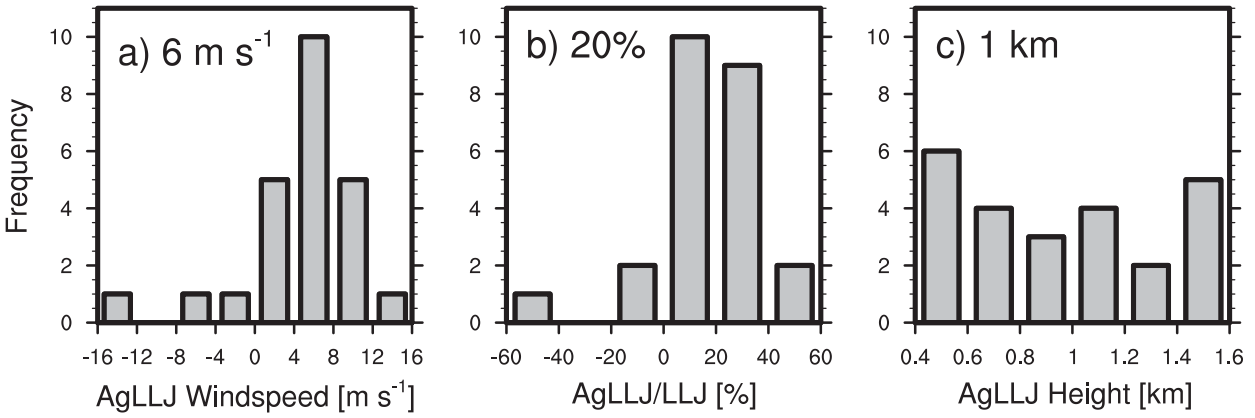

FIG. 4. Histograms of the (a) maximum AgLLJ wind speed ($m\,s^{-1}$), (b) fractional contribution of AgLLJ wind to the total wind (unitless), and (c) height of the AgLLJ (km). The numbers at the top left of each plot are the averages of each quantity for the 21 of 24 positively ageostrophic cases.

95th percentile level that, unlike the previous test, accounts for the magnitude of the ageostrophy. It results in a pattern of statistical significance (not shown) very similar to that of the Boolean test in that both the AgLLJ and the surface subgeostrophy are found to be statistically significant regions. We do not report on field significance since the field in question (transect-normal wind speed) exhibits only two spatial degrees of freedom (Livezey and Chen 1983). This is because the wind speed at the LLJ center grid cell is highly correlated (>0.7) to the wind speed at all other grid cells among the transects.

Figure 4 shows distributions of the transect-normal ageostrophic wind speed, ageostrophic percentage of the total transect-normal wind, and height above sea level of the ageostrophic wind calculated from the LLJ profiles. Since the study is focused on the positive ageostrophy of the LLJ, the averages of each distribution in the upper-left corner of each plot in Fig. 4 do not account for the three cases of negative ageostrophy. For the 21 positively ageostrophic cases, the average transect normal ageostrophy is $6\,m\,s^{-1}$, the percentage of ageostrophy in the total transect normal wind speed is 20%, and the height above sea level of the ageostrophy is 1 km. The distributions provide a sense of variance not incorporated in Fig. 3 and also demonstrate that the composite transects are characteristic of the majority of the samples.

Although the role of the LLJ in transporting water vapor within ARs has been well studied (Neiman et al. 2002, 2009; Ralph et al. 2005; Kingsmill et al. 2013; Cordeira et al. 2013; Valenzuela and Kingsmill 2015), the specific contribution of the ageostrophic wind has not. The average vertical profile of the water vapor transport in the LLJ is shown in the Fig. 5 (normalized in height as in Figs. 2 and 3) for both the transect-normal total and geostrophic components. Above a normalized height of 2, the total and geostrophic profiles are nearly identical; but below this height they are entirely different. The discrepancies result from frictional drag, which reduces the total wind near the surface, and the AgLLJ, which increases the wind centered at a normalized height of 1. The substantial difference in the two profiles demonstrates the important role of the ageostrophy in the water vapor transport.

b. *Gradient wind imbalance*

The geostrophic wind approximation is accurate for only nearly straight flow. Air parcels with highly

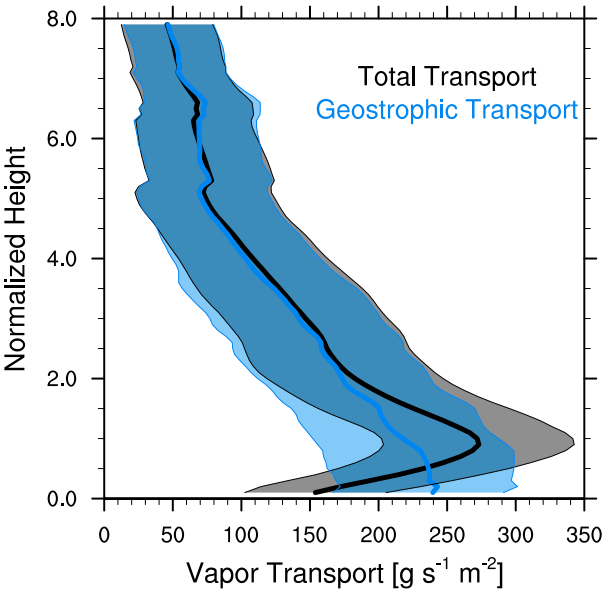

FIG. 5. Transect-normal water vapor transport as a function of height for the total (black; $g\,s^{-1}\,m^{-2}$) and the geostrophic (blue; $g\,s^{-1}\,m^{-2}$) with the averages in bold and one standard deviation shown in color fill. The vertical profiles are taken at the LLJ location. A running vertical mean of 3 points is applied to both curves with only superficial differences compared to the original profiles.

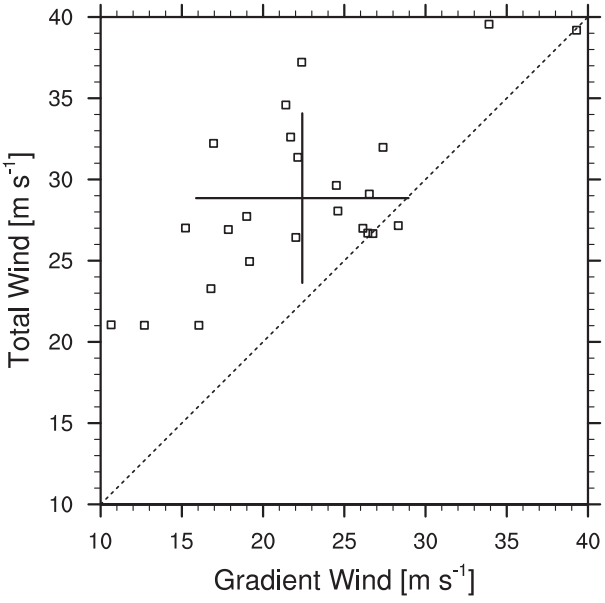

FIG. 6. The observed transect-normal total winds ($m\,s^{-1}$) vs the transect-normal gradient wind for each of the 24 transects. The cross shows the mean at the center and the 1σ standard deviations given by the lengths of each of its axes.

curved trajectories will have an additional component of acceleration acting upon them known as the centrifugal force, which leads to wind directional accelerations but not wind speed accelerations. When examining wind speed accelerations, it is more appropriate to examine the gradient wind rather than the geostrophic wind because the former accounts for curvature effects. While the wind speed accelerations are of ultimate interest here, the present study focuses on the observed ageostrophy rather than the gradient wind imbalance because the latter cannot be calculated from the dropsondes alone due to the lack of air parcel trajectory information.

Figure 6 shows the transect-normal gradient wind speed plotted against total wind speed for the LLJ maxima in each transect. For nearly all cases, the transect-normal total wind speed is greater than the gradient wind speed, indicating that the LLJ is not only supergeostrophic but is also supergradient. The latter is a more powerful statement than the former because it guarantees that the LLJ is undergoing wind speed accelerations while the former may not. This motivates an analysis to understand the dynamics responsible for the observed ageostrophy, which is addressed in section 4.

c. *Comparison of observations with ERA5 reanalysis*

Since the accuracy of the AgLLJ feature depends on the reliability of the geostrophic wind calculation, we now compare the geostrophic winds calculated from dropsondes with those calculated from the ERA5 reanalysis product to determine whether any biases exist, which could create a spurious AgLLJ. The following methods were applied to the ERA5 product to ensure a fair comparison with the observational fields. First, the geostrophic and ageostrophic winds were calculated from the full ERA5 output fields using centered finite differencing. Then, for each transect, the ERA5 fields were temporally interpolated to the hour and minute of the LLJ profile dropsonde and horizontally interpolated to the T-S adjusted location of every dropsonde to form an ERA5 ''dropsonde'' transect. Since it is possible that the ERA5 may not place the LLJ in the same location as in the observations, we applied to the ERA5 ''dropsonde'' transect the same method for finding the LLJ that was applied to the observed dropsonde transect. Finally, a rotation of coordinates was performed in the same manner as for the dropsondes to yield the transect-normal geostrophic, ageostrophic, and total wind fields.

Figure 7a shows a scatterplot of the observed and ERA5 transect-normal geostrophic and total winds at the LLJ for each of the 24 transects. This analysis illustrates a clear low bias in the ERA5 transect normal total wind relative to the observed wind (blue squares) with a mean difference of $5.4\,m\,s^{-1}$ that is statistically significant at the 95th percentile confidence level ($p < 0.05$) using a Welch's t test. Interestingly, no bias is observed in the transect-normal geostrophic wind (red filled circles Fig. 7a), suggesting that the method for calculating the transect-normal geostrophic wind for the dropsondes is reliable. A low bias is also found in the ERA5 ageostrophic winds (not shown) with a mean difference of $5.0\,m\,s^{-1}$ that is statistically significant at the 95th percentile confidence level using a Welch's t test. The fact that the total wind field is biased low by the same amount as the ageostrophic winds (5.4 vs $5.0\,m\,s^{-1}$) suggests that the ERA5 product generally does not resolve the observed AgLLJ feature.

To increase the confidence of these results, a possible methodological flaw is explored and refuted. Since the transect-normal winds were used in the previous analysis, any substantial deviation in the ERA5 wind direction from that of the observed wind will result in an incommensurate comparison. To investigate this possible bias further, the unrotated observed total wind speed is plotted against the unrotated ERA5 total wind speed at the LLJ location (Fig. S2). This compares the strongest possible ERA5 winds with that of the observed winds and eliminates any possibility of a low bias due to orientation. The results (Fig. S2) are similar to that of Fig. 7a such that the ERA5 total wind speeds are biased

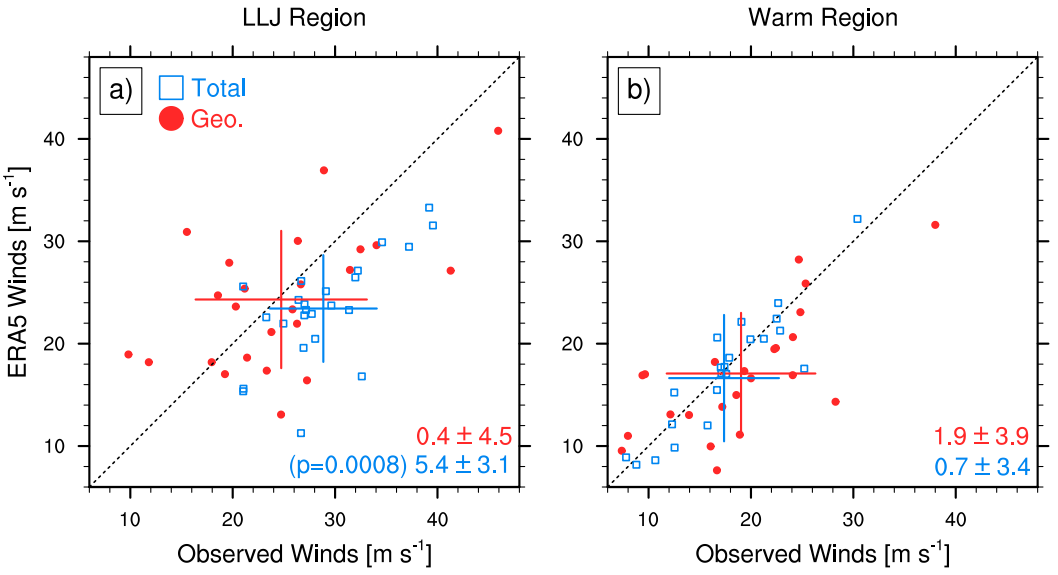

FIG. 7. (a) ERA5 vs the observed transect-normal total wind speed (blue empty squares; m s^{-1}) and transect-normal geostrophic wind speed (red filled circles; m s^{-1}) at the LLJ location, (b) as in (a), but for the warm region as mentioned in the text. The crosses are centered at the mean values with lengths of one standard deviation. The numbers on the bottom right are the difference in the means with a confidence interval at the 95th percentile using a two-tail *t*-test distribution, and the *p* values for a Welch's *t* test in the parentheses.

low by 3.1 m s^{-1} an amount less than in the rotated case suggesting that the wind direction may account for some of the significant differences observed in Fig. 7. This lends further support to the reliability of the methods to determine observed wind.

The preceding evidence suggests that the ERA5 total wind field is biased low because it generally does not resolve the AgLLJ. We now provide further evidence by applying the same methods used to create Fig. 7a to a different region that contains zero ageostrophy to determine if the ERA5 total winds are biased low in that region as they are in the LLJ region. The region selected is dubbed the "warm" region and is located at distance = +200 km and height = 1 in the space of Fig. 3a where the ageostrophic winds are zero in the observed composite. The results, shown in Fig. 7b, plainly illustrate that ERA5 has no statistically significant bias (having p values > 0.1) in either the transect-normal total wind nor geostrophic wind. This supports the hypothesis that the ERA5 LLJ total wind is biased low due to the inability of ERA5 to resolve the AgLLJ feature. This conclusion is consistent with Martin et al. (2018), who found that the WRF and GEFS reforecast models tended to be "too geostrophic" as compared with dropsonde observations in exactly the same region investigated here, which resulted in a low bias in the total wind and water vapor transport. While the ERA5 almost always has a low bias in the transect-normal ageostrophic wind, there is one case that did adequately produce the AgLLJ feature, which will be explored in detail in the next section.

4. Diagnostic analysis for an AgLLJ case study

a. Evolution of the AgLLJ

The 13 February 2016 AR was a very strong event reaching a peak IVT of about 1000 kg m^{-1} s^{-1} (Figs. 1j,k), making it an AR CAT4 upon landfall in the Pacific Northwest, with 4 on a scale of 5 corresponding to "mostly hazardous, also beneficial" (Ralph et al. 2019). The evolution of the alongfront ageostrophy is shown in Fig. 8 where an elongated very narrow band of ageostrophic wind is observed to intensify and decay while propagating southeastward in the span of about 15 h. The ageostrophic wind is rotated to the transect-normal direction, approximately the alongfront direction (see Fig. 8), such that all of the red and orange colors indicate that the ageostrophic wind has at least some southerly or westerly component. At 1200 UTC 13 February, the ageostrophy is primarily cross-frontal, likely driven by the larger-scale transverse circulation, with only a narrow strip of alongfront ageostrophy located immediately ahead of the cold front. Over the next 6 h the strength of the ageostrophy along this strip intensifies over an area having a length on the order of 10^3 km, a width of 10^2 km, and an ageostrophic wind magnitude ranging from 5 to 10 m s^{-1}. These characteristics are consistent with the observed ageostrophy discussed in section 3a. After peak intensity, the strip

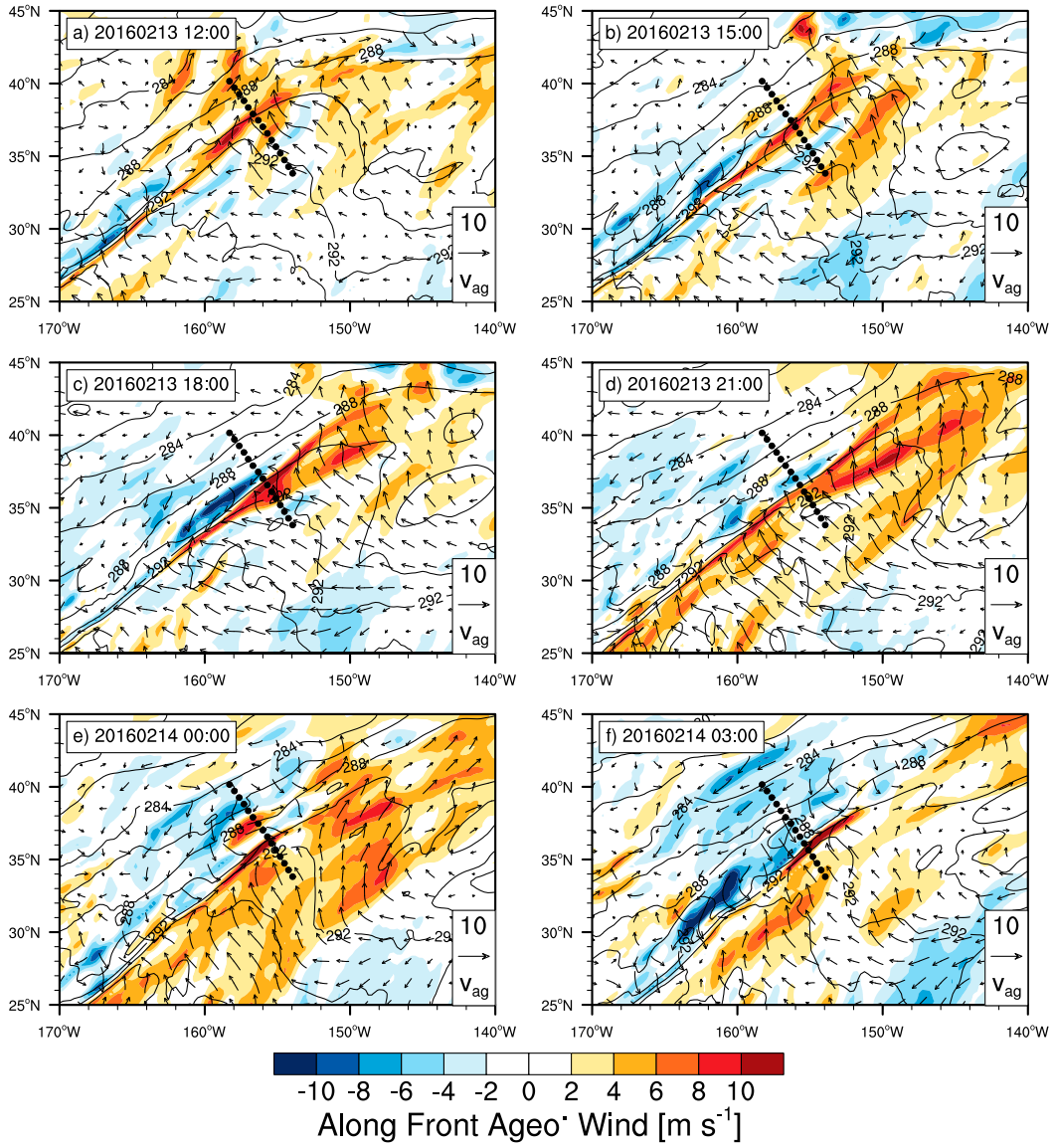

FIG. 8. A 950-hPa time sequence from 1800 UTC 13 Feb to 0900 UTC 14 Feb 2016 of the potential temperature (solid black; K), alongfront ageostrophic winds (color fill; m s^{-1}), and ageostrophic wind vectors (m s^{-1}).

begins to shrink in size until all that is left is a small region at 0300 UTC 14 February.

Figure 9 shows an ERA5 transect taken across the region of maximum ageostrophy occurring at 1800 UTC 13 February and shown in each panel of Fig. 8. The transect exhibits an LLJ and its accompanying alongfront ageostrophic component (i.e., the AgLLJ). This figure is plotted on height levels for consistency with the previous cross sections, which results in some missing values at the surface since ERA5 output is not available on pressure levels below the 1000-hPa level and the surface pressure for this transect is greater than 1000 hPa. From Fig. 9a, the alongfront total wind speed maximum is observed to be about 28 m s^{-1}, centered at 1000 m, found ahead of the cold front, and above the boundary layer. The AgLLJ is found at the same location having a core width of nearly 200 km and magnitude of about 8 m s^{-1}, which agree qualitatively with the observations shown in Fig. 3. Although not shown, both the LLJ and AgLLJ are located within the column of maximum moisture content along the transect above a region of surface convergence and found on the warm side of a low-level potential vorticity anomaly, consistent with the hypothesis that condensational heating leads to an enhancement of the LLJ (Lackmann 2002). These observations are all consistent with the composite

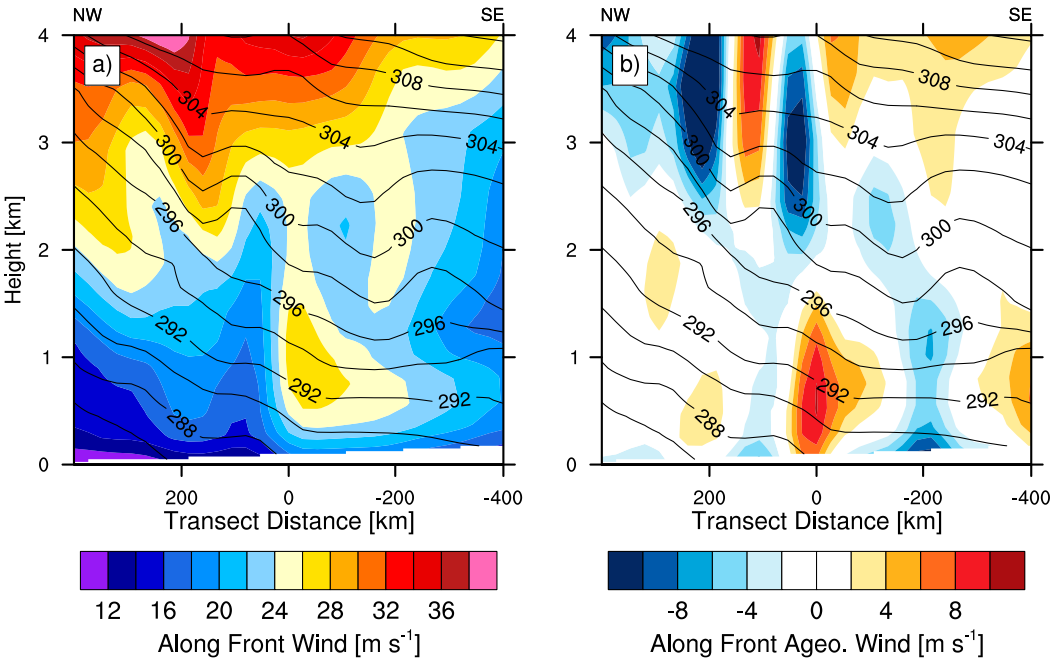

FIG. 9. ERA5 for the transect shown in Fig. 8 of the potential temperature (solid black; K) and (a) transect-normal total wind speed (color fill; m s^{-1}), and (b) transect-normal ageostrophic wind speed (color fill; m s^{-1}). The NW and SE labels at the top represent the northwest and southeast ends of the transect (as shown in Fig. 8).

analysis seen in section 3, although this case study provides an example of more typical gradients in the wind, temperature, and moisture content without the smoothing effect that is inherent in the composites.

b. *Diagnostics of the ageostrophic jet's forcing mechanism*

The frictionless horizontal momentum equations in pressure coordinates are rearranged to diagnose the forcing mechanisms of the AgLLJ in the following form:

$$\frac{\partial \boldsymbol{v}_{\mathrm{ag}}}{\partial t} = -\left(f^{-1}\hat{k}\times\nabla\frac{\partial\phi}{\partial t}\right) - (\boldsymbol{v}\cdot\nabla)\boldsymbol{v} - f\hat{k}\times\boldsymbol{v}_{\mathrm{ag}}, \quad (5)$$

where $\boldsymbol{v}_{\mathrm{ag}}$ is the ageostrophic wind vector, $\boldsymbol{v}$ is the total wind vector, ϕ is the geopotential height, and f is Coriolis parameter. Five terms from (5) are calculated and defined here. The first term represents the lhs of (5) and is dubbed the "time differenced tendency" because it is calculated by taking finite differences in time of the ageostrophic wind field. Terms 2–4 are the "isallobaric tendency," "advective tendency," and "ageostrophic Coriolis torque tendency" corresponding to the three rhs terms, respectively. Finally, the fifth term is the sum of the rhs of (5) and is dubbed the "instantaneous tendency" because it is calculated using data at one instant in time. Each of the five terms are rotated to obtain the alongfront (i.e., transect-normal) components in the same manner as applied in section 4a. The purpose of calculating two estimates of the total tendency (time differenced and instantaneous) is for validation purposes since these two fields are expected to be identical with one another given perfect data. In practice, however, the correlation is imperfect because the time differenced tendency is an average tendency over 3 h while the instantaneous tendency is at a single moment in time. The purpose of calculating the individual forcing terms is to quantify each of their contributions in the AgLLJ.

Each of the five terms calculated from ERA5 for the 950-hPa level are plotted in Fig. 10 for 1500 UTC 13 February while the AgLLJ wind speeds are intensifying. Comparison of the time differenced tendency pattern with the instantaneous tendency pattern shows a qualitatively similar picture with both patterns exhibiting a dipole of positive/negative accelerations at the dropsonde transect location (Figs. 10a,b). The differences in the magnitude between the time difference and instantaneous tendencies exist primarily because they are incommensurate in time but also because friction is neglected in the latter term. Despite the difference in magnitudes, the qualitative agreement between the two terms provides confidence in the forcing components.

Next, the forcing components are examined individually in Figs. 10c–e. The isallobaric term (Fig. 10c) is concentrated along the front and dominated by the strong positive acceleration greater than 1.0×10^{-3} m s^{-2}.

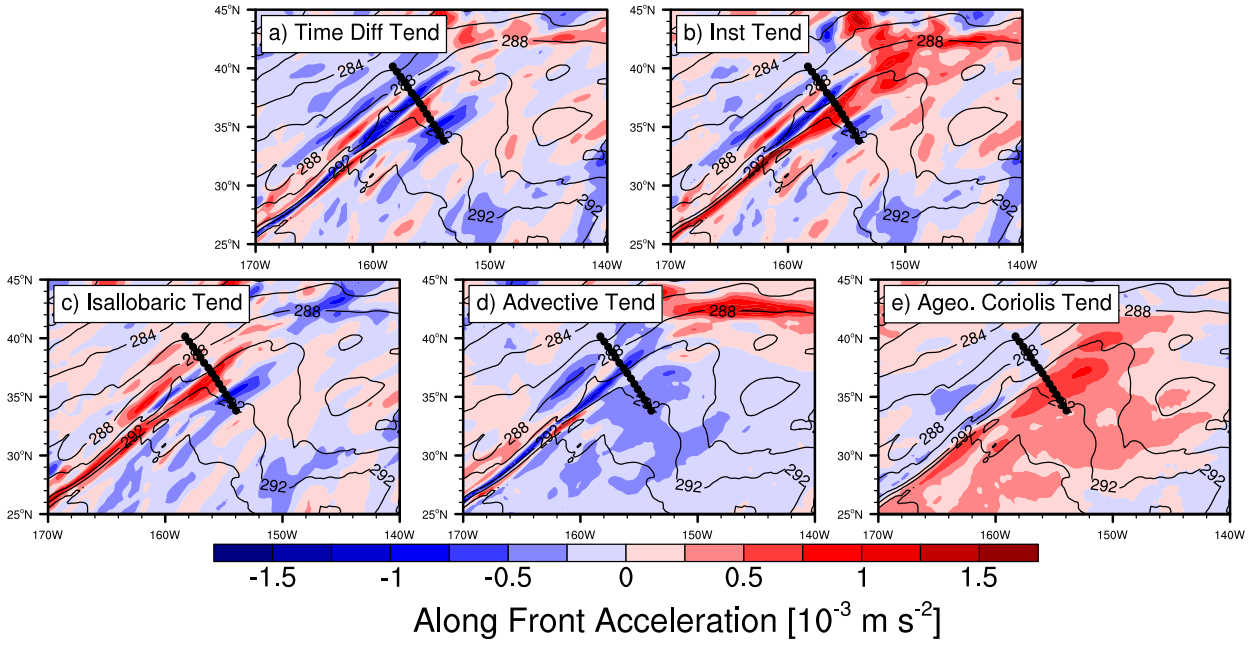

FIG. 10. 950-hPa plan view maps at 1500 UTC 13 Feb of the transect-normal ageostrophic accelerations contributing to (a) the time differenced ageostrophic wind tendency, (b) the instantaneous ageostrophic wind tendency, (c) the isallobaric tendency, (d) advective tendency, and (e) ageostrophic Coriolis torque tendency (color fill; $\mathrm{m\,s^{-2}}$). The potential temperature is shown in solid black every 2 K.

If sustained over only 1 h, the positive acceleration would produce an ageostrophic wind speed of $3.6\,\mathrm{m\,s^{-1}}$, which is consistent with the observed ageostrophic wind speeds from section 3a. The advection tendency term (Fig. 10d) exhibits a strong negative tendency along the front on the order of $-1.0\times10^{-3}\,\mathrm{m\,s^{-2}}$ with a positive tendency strip to the southwest of the transect. It additionally has a much weaker but broader region of negative acceleration extending far out into the warm region. Last, the ageostrophic Coriolis torque tendency term (Fig. 10e) has a very broad positive acceleration extending over the warm region up to the cold front, with some weaker negative acceleration in the cold region.

A qualitatively similar picture is seen in the cross sections (dotted line in Figs. 8 and 10) of the forcing terms shown in Fig. 11. For context, the alongfront ageostrophic winds are overlaid on the cross sections (black contours) and are located immediately ahead of the cold front with a magnitude above $8\,\mathrm{m\,s^{-1}}$ that decays rapidly with height. As in the plan view, there is good agreement between the patterns of time differenced and instantaneous tendencies despite the difference in magnitude. Additionally, the isallobaric and the AgLLJ maxima are collocated with one another indicating that the AgLLJ is being accelerated by the isallobaric term at this time. In contrast, both the minimum advective tendency and the maximum ageostrophic Coriolis torque terms are offset from the AgLLJ maximum indicating that both these terms are propagating the AgLLJ at this time. Additionally, there is a secondary maximum in the isallobaric term that is collocated with ageostrophic Coriolis torque term thereby also serving to propagate the AgLLJ.

The evolution of both the AgLLJ and the momentum budget are shown in Fig. 12 starting from 0600 UTC 13 February and ending on 0600 UTC 14 February across the transect shown in the Fig. 8. Initially, at 0600 UTC 13 February (Figs. 12a–d) there is a clear tripole in the instantaneous tendency dominated by the isallobaric and ageostrophic Coriolis torque terms with only small ageostrophic wind values. By 1200 UTC 13 February (Figs. 12e–h), the positive isallobaric tendency generates the clear AgLLJ in the center of the domain with some contribution from the ageostrophic Coriolis torque. At 1800 UTC 13 February (Figs. 12i–l), the continued overlap of the isallobaric tendency with the AgLLJ maximum serves to further intensity the AgLLJ locally reaching a maximum of about $8\,\mathrm{m\,s^{-1}}$. During this same time, the negative advective tendency on the northwest (left) side and the positive ageostrophic Coriolis torque on the southeast (right) side of the AgLLJ maximum propagate the jet toward the southeast. By 0000 UTC 14 February (Figs. 12m–p) the isallobaric tendency continues to intensify and large values of ageostrophy are generated with a substantial contribution from the advective tendency. Finally, by 0600 UTC

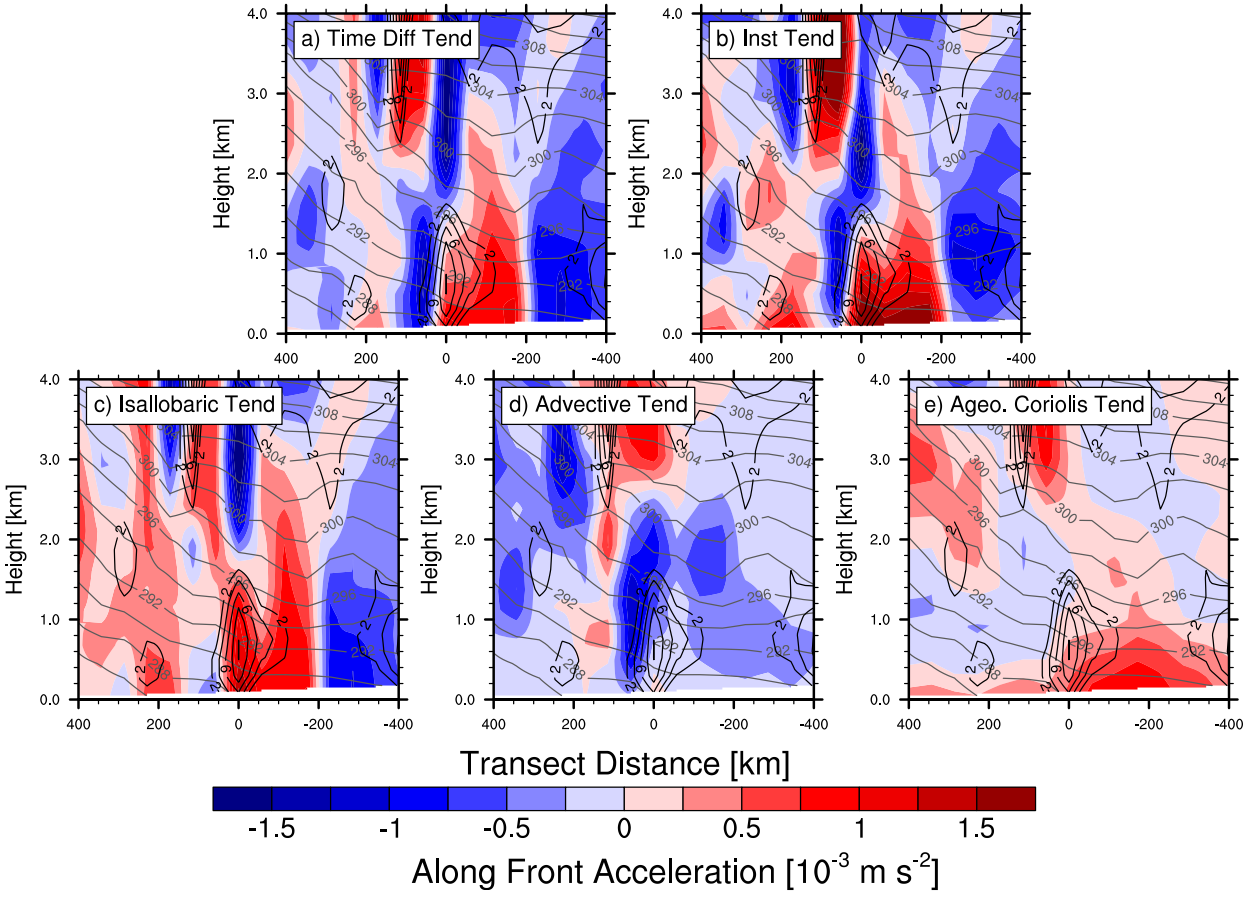

FIG. 11. As in Fig. 10, but with terms calculated along the transects shown in Figs. 8 and 10. The solid black contours are the transect normal ageostrophic winds every 2 m s^{-1} and the solid gray contours are the potential temperatures every 2 K. The left side of each plot is on the northwest side of the transect.

14 February (Figs. 12q–t) negative values in the advective tendency deteriorate the remaining ageostrophy.

The momentum budget analysis demonstrates that the isallobaric tendency is the most concentrated and has the best overlap with the AgLLJ maximum, though there are certainly some contributions from the advective and ageostrophic Coriolis torque tendencies. At low levels ahead of the cold front, the ageostrophic Coriolis torque is broad, weak, and located ahead of the AgLLJ maximum, which serves to propagate rather than intensify the jet. Similarly, the advective tendency is generally negative behind the AgLLJ maximum also serving to propagate the jet. For this case, the observed AgLLJ is found to be driven primarily by the isallobaric tendency and is propagated toward the southeast by the all three tendency terms.

5. Conclusions and discussion

This study employed a large number of aircraft dropsonde observations sampled across atmospheric rivers (AR) to investigate the ageostrophic component of the wind in the transect-normal (i.e., along frontal) direction. It was found that 21 of 24 cases have a positive component of ageostrophic wind with an average magnitude of 6 ± 1.5 m s^{-1}, which contributes about 20% of the total wind at the LLJ maximum located at approximately 1-km elevation. The ageostrophic component of the LLJ, referred to as the AgLLJ, is found immediately ahead of the cold front and above a region of low-level convergence. The question of whether the AgLLJ is an artifact resulting from the neglect of curvature effects in the geostrophic approximation was investigated by calculating the gradient wind, and it was demonstrated that the total wind is greater than the gradient wind in the majority of cases. This indicates that the AgLLJ is also a region of supergradient wind, thus implying that the ageostrophy results from acceleration of wind speed rather than merely directional acceleration associated with gradient wind balance.

The ERA5 reanalysis product was employed to diagnose the forcing dynamics of the AgLLJ. For the majority of the cases investigated here, the ERA5 does

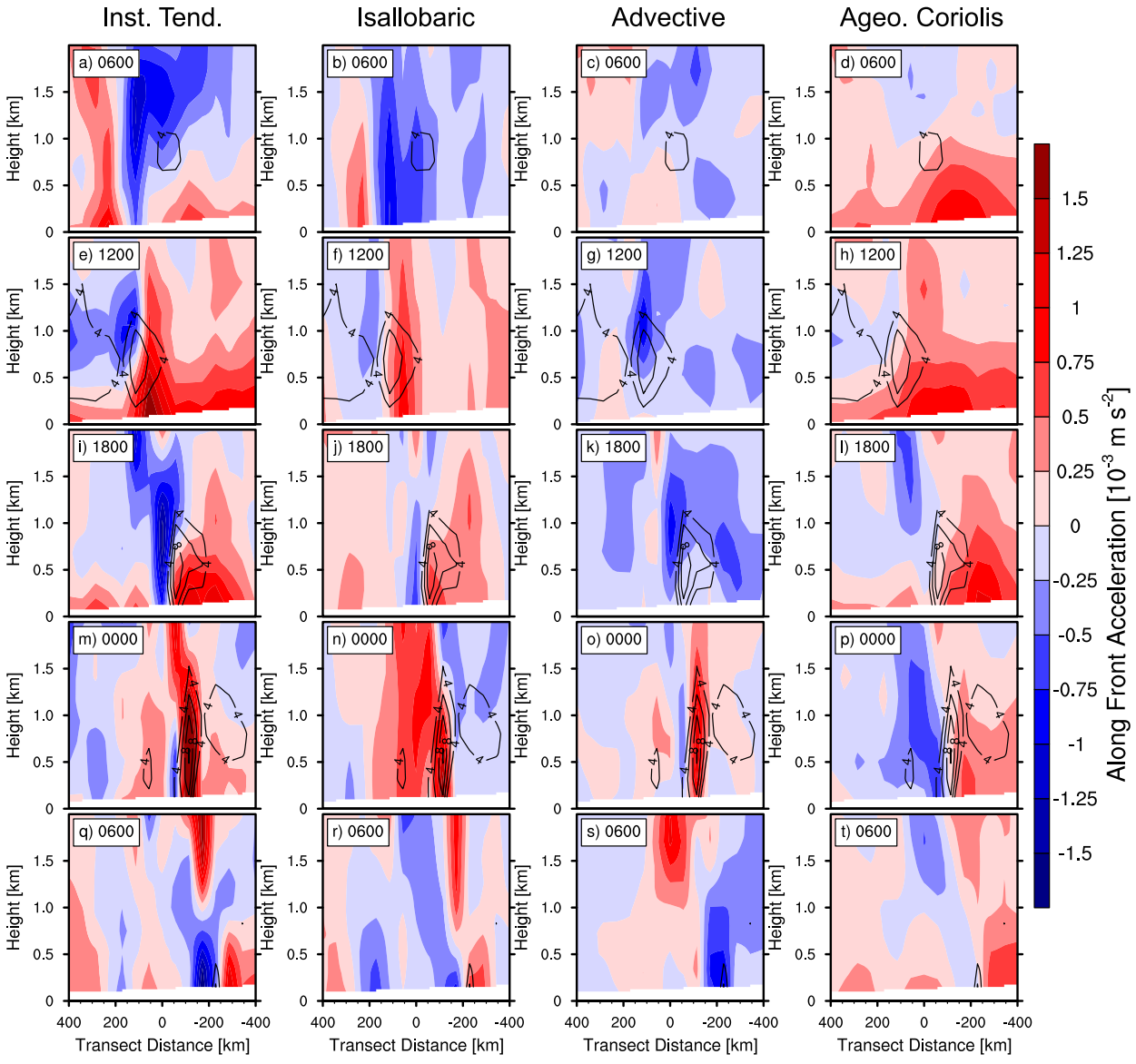

FIG. 12. A time sequence of the momentum budget from 0600 UTC 13 Feb to 0600 UTC 14 Feb for the transect shown in Fig. 8. Each column contains a different term in the momentum budget with column 1 being the instantaneous tendency (Inst Tend), column 2 the isallobaric tendency (Isallobaric), column 3 the advective tendency (Advective), and column 4 the ageostrophic Coriolis torque on the ageostrophic wind (Ageo. Coriolis). The ageostrophic wind normal to the transect is plotted in each plot with a contour interval of 1 m s^{-1} beginning from 4 m s^{-1}.

not adequately resolve the AgLLJ, likely due to the jet's narrow width being on the order of 10^2 km. A one-to-one comparison of the ERA5 and observed geostrophic and total winds demonstrated that the ERA5 has a low bias for the total wind but not the geostrophic wind. One case in which the ERA5 qualitatively reproduces the observed AgLLJ occurs on 13 February 2016. An idealization of the dynamical processes for this case is shown in the Fig. 13 schematic on a 900-hPa plan view surface during the time of maximum AgLLJ intensity. In this schematic, the isallobaric term is collocated with the AgLLJ maximum serving to accelerate the jet. The Coriolis torque term, however, is positive ahead of the jet serving more to propagate the jet toward the southeast rather than to accelerate it. Last, the advection tendency term is found to be negative behind the jet also serving to propagate it toward the southeast.

The positive contribution from the isallobaric tendency term implies that the frontal dynamical processes generating pressure tendencies at low levels lead to a

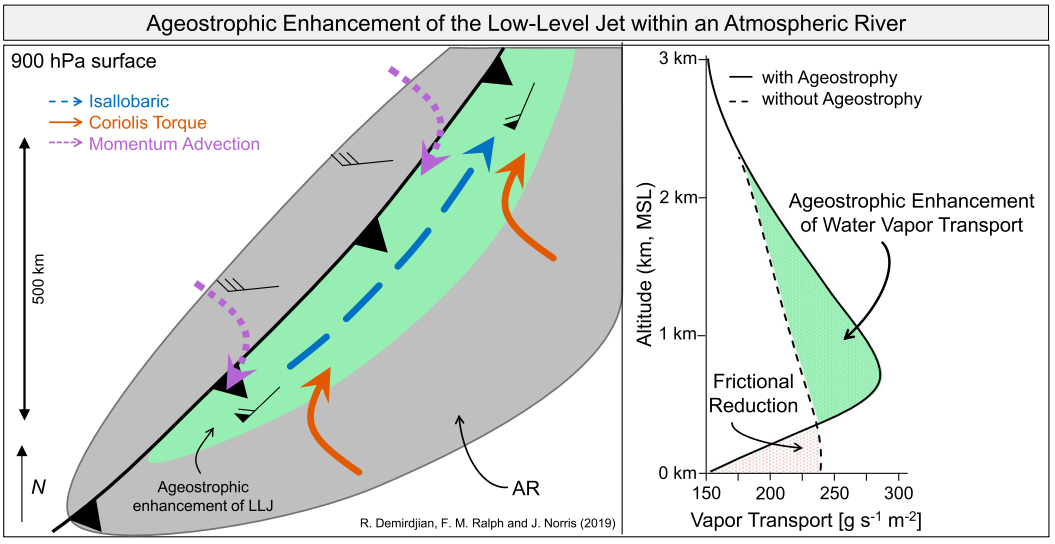

FIG. 13. A conceptual representation of the enhancement (green) of water vapor transport within the low-level jet due to the ageostrophic winds and the dynamical processes serving to accelerate/decelerate the ageostrophic wind. A 900-hPa plan view representation of the forcing mechanisms is shown on the left with the cold front in bold black with triangles, IVT exceeding 250 kg m^{-1} s^{-1} in gray indicating the AR boundaries, and the ageostrophic enhancement of the LLJ in green. The total wind vectors are shown as wind barbs in knots. The acceleration/deceleration vectors are shown with the isallobaric term in long dashed blue, Coriolis torque in solid orange, and momentum advection in short dashed lavender. A vertical profile of the moisture transport is shown on the right and is representative of any position within the green on the plan view.

positive along-frontal ageostrophic wind. This validates the scaling argument from Wakimoto and Murphey (2008) and is consistent with the diagnostic analyses of Uccellini and Johnson (1979), Brill et al. (1985), and Chen et al. (1994). An example of one such process is latent heating above the AgLLJ that may contribute toward pressure falls thereby accelerating the ageostrophic winds. Lackmann (2002) described a related process by which the low-level latent heating generates a diabatically driven PV anomaly to which the horizontal circulation responds by developing a southerly/northerly component on the southeast/northwest side of the PV. By performing a PV inversion analysis, Lackmann was able to quantify the height (pressure) falls associated with the diabatic PV anomaly. Both the isallobaric mechanism from this study and the response to the diabatic PV anomaly from Lackmann (2002) describe a response of the wind due to pressure (height) falls. It thereby seems plausible that they both describe the same response viewed from different frameworks.

The ageostrophic enhancement of the vertical profile of water vapor transport within the LLJ is furthermore illustrated in the Fig. 13 schematic that is based on observed differences between total and geostrophic water vapor transport. Much of the ageostrophic enhancement occurs between 750 and 1250 m, the layer that is known to correlate highly with orographic precipitation (Neiman et al. 2002, 2009). This means that the ageostrophic component adds vapor transport where it is most able to enhance orographic precipitation for the U.S. West Coast during the wet season (fall–spring). Furthermore, without this enhancement the geostrophic component lacks the sharp maximum in the vapor transport profile located at 750 m. Contrastingly, the ageostrophic component actually serves to reduce the vapor transport at the surface, likely due to friction. However, since the elevated enhancement of vapor transport is greater its reduction at the surface, the IVT is increased. Outside of the LLJ region, the wind is expected to be either mostly geostrophic or governed by transverse circulation dynamics. However, inside this region the ageostrophy provides a substantial contribution toward the water vapor transport consistent with Winters and Martin (2014), who found that a large contribution of the vapor transport was associated with the ageostrophy.

Acknowledgments. This project was supported by California's Department of Water Resources.

REFERENCES

American Meteorological Society, 2017: Atmospheric river. Glossary of Meteorology, http://glossary.ametsoc.org/wiki/Atmospheric_River.

Brill, K. F., 2014: Revisiting an old concept: The gradient wind. *Mon. Wea. Rev.*, **142**, 1460–1471, https://doi.org/10.1175/MWR-D-13-00088.1.

——, L. W. Uccellini, R. P. Burkhart, T. T. Warner, and R. A. Anthes, 1985: Numerical simulations of a transverse indirect

circulation and low-level jet in the exit region of an upper-level jet. *J. Atmos. Sci.*, **42**, 1306–1320, https://doi.org/10.1175/1520-0469(1985)042<1306:NSOATI>2.0.CO;2.

Browning, K., and C. W. Pardoe, 1973: Structure of low-level jet streams ahead of mid-latitude cold fronts. *Quart. J. Roy. Meteor. Soc.*, **99**, 619–638, https://doi.org/10.1002/qj.49709942204.

Chen, Y., X. A. Chen, and Y. Zhang, 1994: A diagnostic study of the low-level jet during TAMEX IOP 5. *Mon. Wea. Rev.*, **122**, 2257–2284, https://doi.org/10.1175/1520-0493(1994)122<2257:ADSOTL>2.0.CO;2.

Cordeira, J. M., F. M. Ralph, and B. J. Moore, 2013: The development and evolution of two atmospheric rivers in proximity to western North Pacific tropical cyclones in October 2010. *Mon. Wea. Rev.*, **141**, 4234–4255, https://doi.org/10.1175/MWR-D-13-00019.1.

——, ——, A. Martin, N. Gaggini, J. R. Spackman, P. J. Neiman, J. J. Rutz, and R. Pierce, 2017: Forecasting atmospheric rivers during CalWater 2015. *Bull. Amer. Meteor. Soc.*, **98**, 449–459, https://doi.org/10.1175/BAMSB33-D-15-00245.1.

Dettinger, M. D., 2013: Atmospheric rivers as drought busters on the U.S. West Coast. *J. Hydrometeor.*, **14**, 1721–1732, https://doi.org/10.1175/JHM-D-13-02.1.

——, F. M. Ralph, T. Das, P. J. Neiman, and D. R. Cayan, 2011: Atmospheric rivers, floods and the water resources of California. *Water*, **3**, 445–478, http://doi.org/10.3390/w3020445.

Dudhia, J., 1993: A nonhydrostatic version of the Penn State–NCAR mesoscale model: Validation tests and simulation of an Atlantic cyclone and cold front. *Mon. Wea. Rev.*, **121**, 1493–1513, https://doi.org/10.1175/1520-0493(1993)121<1493:ANVOTP>2.0.CO;2.

European Centre for Medium-Range Weather Forecasts, 2017: ERA5 reanalysis. National Center for Atmospheric Research, Computational and Information Systems Laboratory, accessed 7 September 2019, https://doi.org/10.5065/D6X34W69.

Guan, B., and D. E. Waliser, 2015: Detection of atmospheric rivers: Evaluation and application of an algorithm for global studies. *J. Geophys. Res. Atmos.*, **120**, 12 514–12 535, https://doi.org/10.1002/2015JD024257.

Kingsmill, D. E., P. J. Neiman, B. J. Moore, M. Hughes, S. E. Yuter, and F. M. Ralph, 2013: Kinematic and thermodynamic structures of Sierra barrier jets and overrunning atmospheric rivers during a landfalling winter storm in northern California. *Mon. Wea. Rev.*, **141**, 2015–2036, https://doi.org/10.1175/MWR-D-12-00277.1.

Lackmann, G. M., 2002: Cold-frontal potential vorticity maxima, the low-level jet, and moisture transport in extratropical cyclones. *Mon. Wea. Rev.*, **130**, 59–74, https://doi.org/10.1175/1520-0493(2002)130<0059:CFPVMT>2.0.CO;2.

——, and J. Gyakum, 1999: Heavy cold-season precipitation in the northwestern United States: Synoptic climatology and an analysis of the flood of 17–18 January 1986. *Wea. Forecasting*, **14**, 687–700, https://doi.org/10.1175/1520-0434(1999)014<0687:HCSPIT>2.0.CO;2.

Lavers, D. A., R. P. Allan, E. F. Wood, G. Villarini, D. J. Brayshaw, and A. J. Wade, 2011: Winter floods in Britain are connected to atmospheric rivers. *Geophys. Res. Lett.*, **38**, L23803, https://doi.org/10.1029/2011GL049783.

Livezey, R. E., and W. Y. Chen, 1983: Statistical field significance and its determination by Monte Carlo techniques. *Mon. Wea. Rev.*, **111**, 46–59, https://doi.org/10.1175/1520-0493(1983)111<0046:SFSAID>2.0.CO;2.

Martin, A., F. M. Ralph, R. Demirdjian, L. DeHaan, R. Weihs, J. Helly, D. Reynolds, and S. Iacobellis, 2018: Evaluation of atmospheric river predictions by the WRF Model using aircraft and regional mesonet observations of orographic precipitation and its forcing. *J. Hydrometeor.*, **19**, 1097–1113, https://doi.org/10.1175/JHM-D-17-0098.1.

Moore, B. J., P. J. Neiman, F. M. Ralph, and F. Barthold, 2012: Physical processes associated with heavy flooding rainfall in Nashville, Tennessee and vicinity during 1–2 May 2012: The role of an atmospheric river and mesoscale convective systems. *Mon. Wea. Rev.*, **140**, 358–378, https://doi.org/10.1175/MWR-D-11-00126.1.

Neiman, P. J., F. M. Ralph, A. White, D. Kingsmill, and P. Persson, 2002: The statistical relationship between upslope flow and rainfall in California' s coastal mountains: Observations during CALJET. *Mon. Wea. Rev.*, **130**, 1468–1492, https://doi.org/10.1175/1520-0493(2002)130<1468:TSRBUF>2.0.CO;2.

——, ——, G. A. Wick, J. Lundquist, and M. D. Dettinger, 2008: Meteorological characteristics and overland precipitation impacts of atmospheric rivers affecting the West Coast of North America based on eight years of SSM/I satellite observations. *J. Hydrometeor.*, **9**, 22–47, https://doi.org/10.1175/2007JHM855.1.

——, D. J. Gottas, A. B. White, S. I. Gutman, and F. M. Ralph, 2009: A water vapour flux tool for precipitation forecasting. *Proc. Inst. Civ. Eng.: Water Manage.*, **162**, 83–94, https://doi.org/10.1680/WAMA.2009.162.2.

——, G. A. Wick, B. J. Moore, F. M. Ralph, J. R. Spackman, and B. Ward, 2014: An airborne study of an atmospheric river over the subtropical Pacific during WISPAR: Dropsonde budget-box diagnostics and precipitation impacts in Hawaii. *Mon. Wea. Rev.*, **142**, 3199–3223, https://doi.org/10.1175/MWR-D-13-00383.1.

Orlanski, I., and B. Ross, 1977: The circulation associated with a cold front. Part I: Dry case. *J. Atmos. Sci.*, **34**, 1619–1633, https://doi.org/10.1175/1520-0469(1977)034<1619:TCAWAC>2.0.CO;2.

Ralph, F. M., P. J. Neiman, and R. Rotunno, 2005: Dropsonde observations in low-level jets over the northeastern Pacific Ocean from CALJET-1998 and PACJET-2001: Mean vertical-profile and atmospheric-river characteristics. *Mon. Wea. Rev.*, **133**, 889–910, https://doi.org/10.1175/MWR2896.1.

——, ——, G. A. Wick, S. I. Gutman, M. D. Dettinger, D. R. Cayan, and A. B. White, 2006: Flooding on California's Russian River: Role of atmospheric rivers. *Geophys. Res. Lett.*, **33**, L13801, https://doi.org/10.1029/2006GL026689.

——, and Coauthors, 2016: CalWater field studies designed to quantify the roles of atmospheric rivers and aerosols in modulating U.S. West Coast precipitation in a changing climate. *Bull. Amer. Meteor. Soc.*, **97**, 1209–1228, https://doi.org/10.1175/BAMS-D-14-00043.1.

——, and Coauthors, 2017: Dropsonde observations of total integrated water vapor transport within North Pacific atmospheric rivers. *J. Hydrometeor.*, **18**, 2577–2596, https://doi.org/10.1175/JHM-D-17-0036.1.

——, J. J. Rutz, J. M. Cordeira, M. Dettinger, M. Anderson, D. Reynolds, L. J. Schick, and C. Smallcomb, 2019: A scale to characterize the strength and impacts of atmospheric rivers. *Bull. Amer. Meteor. Soc.*, **100**, 269–289, https://doi.org/10.1175/BAMS-D-18-0023.1.

Rutz, J. J., W. J. Steenburgh, and F. M. Ralph, 2014: Climatological characteristics of atmospheric rivers and their inland penetration over the western United States. *Mon. Wea. Rev.*, **142**, 905–921, https://doi.org/10.1175/MWR-D-13-00168.1.

Thorpe, A., and S. Clough, 1991: Mesoscale dynamics of cold fronts: Structures described by dropsoundings in FRONTS.

Quart. J. Roy. Meteor. Soc., **117**, 903–941, https://doi.org/10.1002/qj.49711750103.

Uccellini, L. W., and D. R. Johnson, 1979: The coupling of upper and lower tropospheric jet streaks and implications for the development of severe convective storms. *Mon. Wea. Rev.*, **107**, 682–703, https://doi.org/10.1175/1520-0493(1979)107<0682:TCOUAL>2.0.CO;2.

Valenzuela, R. A., and D. E. Kingsmill, 2015: Orographic precipitation forcing along the coast of northern California during a landfalling winter storm. *Mon. Wea. Rev.*, **143**, 3570–3590, https://doi.org/10.1175/MWR-D-14-00365.1.

Wakimoto, R., and H. Murphey, 2008: Airborne Doppler radar and sounding analysis of an oceanic cold front. *Mon. Wea. Rev.*, **136**, 1475–1491, https://doi.org/10.1175/2007MWR2241.1.

Winters, A. C., and J. E. Martin, 2014: The role of a polar/subtropical jet superposition in the May 2010 Nashville flood. *Wea. Forecasting*, **29**, 954–974, https://doi.org/10.1175/WAF-D-13-00124.1.